OPEN ACCESS



Detecting Preheating in Protoclusters with Ly α Forest Tomography

Robin Kooistra 1 , Shigeki Inoue 2,3,4 , Khee-Gan Lee 1 , Renyue Cen 5 , and Naoki Yoshida 1,6,7
Kavli IPMU (WPI), UTIAS, The University of Tokyo, Kashiwa, Chiba 277-8583, Japan
Center for Computational Sciences, University of Tsukuba, Ten-nodai, 1-1-1 Tsukuba, Ibaraki 305-8577, Japan
Chile Observatory, National Astronomical Observatory of Japan, Mitaka, Tokyo 181-8588, Japan
Department of Cosmosciences, Graduates School of Science, Hokkaido University, Sapporo, Hokkaido 060-0810, Japan Department of Physics, School of Sciences, Princeton University, Princeton, NJ 08544, USA
Department of Physics, School of Science, The University of Tokyo, Bunkyo, Tokyo 113-0033, Japan
Institute for Physics of Intelligence, School of Science, The University of Tokyo, 7-3-1 Hongo, Bunkyo, Tokyo 113-0033, Japan
Received 2021 September 20; revised 2021 December 20; accepted 2022 January 17; published 2022 March 4

Abstract

Studies of low-redshift galaxy clusters suggest the intracluster medium (ICM) has experienced nongravitational heating during the formation phase of the clusters. Using simple phenomenological heating prescriptions, we simulate the effect of this preheating of the nascent ICM in galaxy protoclusters and examine its effect on Ly α forest tomographic maps. We analyze a series of cosmological zoom-in simulations of protoclusters within the framework of the Ly α transmission—dark matter (DM) density distribution. We find that the more energy is injected into the proto-ICM at z=3, the more the distribution at high DM density tilts toward higher Ly α transmission. This effect has been confirmed in both low-resolution simulations adopting a preheating scheme based on entropy floors, as well as in higher-resolution simulations with another scheme based on energy floors. The evolution of the slope of this distribution is shown to vary with redshift. The methodology developed here can be applied to current and upcoming Ly α forest tomographic survey data to help constrain feedback models in galaxy protoclusters.

Unified Astronomy Thesaurus concepts: Galaxy clusters (584); Intracluster medium (858); Lyman alpha forest (980)

1. Introduction

According to the hierarchical structure formation scenario, galaxy clusters are expected to form through gravitational collapse, where galaxies, galaxy groups, and small clusters merge to form increasingly more massive structures. However, even in early X-ray observations of galaxy clusters, it was found that the slope of the X-ray luminosity-temperature relation can be much steeper than the predicted slope of 2 expected from clusters evolving solely through self-similarity (Kaiser 1986; Edge & Stewart 1991; Markevitch 1998). In order to explain this steeper slope, self-similarity needs to be broken and the intracluster medium (ICM) gas needs to be heated early on by nongravitational sources (e.g., Evrard & Henry 1991). This has become known in the field as "cluster preheating." Support for the preheating scenario has additionally been found in measurements of the entropy in cluster cores (Pratt et al. 2010; Chaudhuri et al. 2013; Iqbal et al. 2017), suggesting that something is heating up the intracluster gas in the early stages of the cluster formation, likely during the "Cosmic Noon" epoch of peak star formation and active galactic nucleus (AGN) activity at $z \sim 3$.

The origin of the preheating of the ICM is still the subject of debate, and several possibilities have been explored. These include energy injection by star formation through supernova feedback, although the amount of energy supernovae can transport is likely insufficient (Loewenstein 2000; Menci & Cavaliere 2000; Bower et al. 2001). Therefore, the major contributor to the preheating is thought to be black hole

Original content from this work may be used under the terms of the Creative Commons Attribution 4.0 licence. Any further distribution of this work must maintain attribution to the author(s) and the title of the work, journal citation and DOI.

feedback from AGNs (Valageas & Silk 1999; Wu et al. 2000; Chaudhuri et al. 2012). The preheating scenario has also been implemented in multiple numerical simulations of clusters (e.g., Navarro et al. 1995; Borgani et al. 2001), as well as the intergalactic medium (IGM; Borgani & Viel 2009), helping to narrow down the possible mechanisms that may lie behind the nongravitational heat injection. Recently, a radio AGN has been found in a protocluster at redshift z = 3.3 (Shen et al. 2021), which adds to the growing consensus that black hole feedback already plays a significant role in the early stages of the evolution of the ICM.

One of the strong probes of heating of intergalactic gas is its neutral hydrogen (H I) content. At high redshift, the IGM can be probed through the Ly α forest absorption features in the spectra of background galaxies and quasars (e.g., Lynds 1971; Meiksin 2009; McQuinn 2016). The observed transmission Fof the absorption features relates to the optical depth $\tau_{\rm Lv}\alpha$ through $F \equiv \exp(-\tau_{\text{Ly}\alpha})$. The optical depth in turn depends on the HI density, which itself can be written as a combination of the HI fraction and the underlying dark matter (DM) density field. The heating processes and astrophysics dominate the evolution of the neutral fraction (e.g., McDonald et al. 2000, 2005; Kollmeier et al. 2006; Arinyo-i-Prats et al. 2015; Tonnesen et al. 2017), whereas the density field depends primarily on the cosmology. In this manner, the Ly α forest has been shown to be a good tracer of the underlying DM density (e.g., Cen et al. 1994; Zhang et al. 1995; Hernquist et al. 1996; Miralda-Escudé et al. 1996) and can thus be used to directly constrain cosmological models either by itself or by combining the Ly α forest with other probes (e.g., Mandelbaum et al. 2003; Seljak et al. 2006; de Sainte Agathe et al. 2019). Global statistics of the Ly α forest, such as the one-dimensional transmission power spectrum and the probability distribution

function (PDF), have been shown to be relatively insensitive to the specific physics of galaxy and AGN feedback (e.g., Lee & Spergel 2011; Viel et al. 2013; Chabanier et al. 2020) with effects of only several percent. Similarly, with the Lagrangian progenitors of modern-day galaxy clusters occupying no more than $\sim\!2\%$ –3% of the total cosmic volume at $z\sim\!2$ –3 (Chiang et al. 2017), any preheating of the proto-ICM during this epoch is expected to have only a small effect on global Ly α forest statistics.

By combining a large sample of multiple $Ly\alpha$ forest sightlines within a small area of the sky, it becomes possible to reconstruct three-dimensional maps of the large-scale structure in absorption (Pichon et al. 2001; Caucci et al. 2008) in a technique known as " $Ly\alpha$ forest tomography." However, quasars—the traditional background probes of the $Ly\alpha$ forest—are relatively scarce on the sky, generally resulting in large transverse sightline separations of roughly tens of h^{-1} Mpc. This makes it challenging to study large-scale structure in detail, but it does allow for the identification of large overdensities and thus protocluster candidates (e.g., Stark et al. 2015; Cai et al. 2016, 2017; Ravoux et al. 2020). Nevertheless, subsequent detailed analysis of the properties of these quasar-identified protoclusters remains challenging due to the low effective resolution of the $Ly\alpha$ sampling (although see Liang et al. 2021).

As shown by Lee et al. (2014a), the area density of Ly α sightlines, and thus the resolution of the reconstructed tomographic maps, can be improved by additionally exploiting the Ly α forest in the spectra of Lyman-break galaxies (LBGs). This makes it possible to reduce the mean sightline separation to scales of a few h^{-1} Mpc (Lee et al. 2014b). The first dedicated large-scale tomographic survey employing the addition of LBGs was the COSMOS Lyman Alpha Mapping And Tomographic Observations (CLAMATO) survey (Lee et al. 2018). This survey covers the COSMOS field with 240 LBG sightlines corresponding to an area of $\sim 0.2 \text{ deg}^2$. A more recent effort called the Lyman Alpha Tomography IMACS Survey (LATIS) covers a larger area of 1.7 deg², although at a slightly lower resolution than CLAMATO (Newman et al. 2020). In a recent work, Nagamine et al. (2021) showed that tomographic surveys such as the ones discussed above, as well as upcoming surveys with the Subaru Prime Focus Spectrograph (PFS; Takada et al. 2014), can be used to probe different models of star formation and supernova feedback, focusing mainly on the one-dimensional statistics of the IGM and the flux contrast in the vicinity of galaxies.

Another recent advance in large-scale structure analysis was one of the motivating factors for this study, namely the application of density reconstruction and constrained realization techniques to high-redshift data sets (Ata et al. 2021). With careful characterization of selection functions and modeling of the galaxy bias, Ata et al. (2021) was able to combine multiple galaxy spectroscopic surveys in the COSMOS field to reconstruct the 3D matter density field at 1.6 < z < 3.2 with an effective resolution of several megaparsecs. Since this matter map overlaps spatially with the Ly α transmission maps from CLAMATO, it presents the unique opportunity to *directly* study the relationship between the Ly α forest and the underlying matter density field. This allows us to test the socalled fluctuating Gunn-Peterson approximation (FGPA; e.g., Croft et al. 1998; Weinberg et al. 2003; Rorai et al. 2013), which predicts a quasi-power-law relationship between the Ly α optical depth and the underlying matter density. However, in

Table 1 Masses at z = 0, z = 2, and z = 3 for the Clusters in the Zoom-in Simulations without Any Preheating Implemented

Cluster halo ID	$M_{ m halo}^{z=0} \ (h^{-1} M_{\odot})$	$M_{ m halo}^{z=2} \ (h^{-1} M_{\odot})$	$M_{\text{halo}}^{z=3} (h^{-1} M_{\odot})$
H1	1.4×10^{15}	4.7×10^{13}	2.4×10^{13}
H2	9.9×10^{14}	6.9×10^{13}	1.8×10^{13}
L1	5.3×10^{14}	2.7×10^{13}	1.1×10^{13}
L2	4.2×10^{14}	2.3×10^{13}	8.0×10^{12}
L3	3.9×10^{14}	2.7×10^{13}	6.5×10^{12}

Note. Masses were determined using the FoF algorithm.

known protocluster regions (readily identifiable as extended overdensities in both the $Ly\alpha$ and matter density maps), cluster preheating should manifest itself as deviations from the global FGPA in protocluster regions.

Recently, Miller et al. (2021) analyzed protoclusters in the Illustris TNG100 hydrodynamical simulation and studied the effect of AGNs on the thermal and ionization properties. They found that an AGN affects the Ly α transmission within $\sim 1~h^{-1}$ Mpc of the central halo at $z\sim 2.4$, but the effects are minor when smoothed over the $\geqslant 4~h^{-1}$ Mpc scales typically used to search for protoclusters in the Ly α forest. However, this study was limited to the relatively low-mass protoclusters $M<10^{14.4}~h^{-1}~M_{\odot}$ and did not consider the possibility of studying the Ly α transmission as a function of the underlying density field.

In this paper, we build upon such studies and examine more specifically the effect of cluster preheating in the protocluster gas on the Ly α forest absorption field of the proto-ICM at $2\leqslant z\leqslant 3$, as a function of the underlying matter overdensity. In this redshift range, it might be possible to directly detect any preheating of the ICM gas right around the time the energy injection is ongoing. This would help to more directly constrain the different preheating mechanisms that have been proposed to explain the observed cluster properties at lower redshifts.

In order to encapsulate a range of cluster masses, we ran zoomin simulations of protocluster regions both with and without preheating of the gas and examine the effect in the framework of the distribution of $\text{Ly}\alpha$ transmission as a function of DM density. This distribution can be probed directly in the near future by using the currently available large tomographic surveys where information on the DM density field is also available.

We present the details of the simulations and how they were processed, as well as the models for preheating adopted in this work in Section 2. The resulting Ly α transmission—DM density distribution is then presented in the results in Section 3 and we discuss its implications for applying the framework developed here to observations in Section 3.3.

2. Simulations

Initial conditions of our cosmological simulations are created with the publicly open code MULTI-SCALE INITIAL CONDITIONS (MUSIC; Hahn & Abel 2011). Our adopted cosmological parameters are $\Omega_{\rm m}=0.28$, $\Omega_{\rm b}=0.045$, and $\Omega_{\Lambda}=0.72$ with a Hubble constant $H_0=100\,h\,{\rm km\,s^{-1}\,Mpc^{-1}}$, where h=0.70. Simulations are performed in two steps. First, we use an *N*-body simulation preformed with a uniform and coarse resolution for a large volume with a comoving side length of $300\,h^{-1}\,{\rm Mpc}$. From the output of this simulation at redshift z=0, we identify five halos containing massive clusters with various masses that

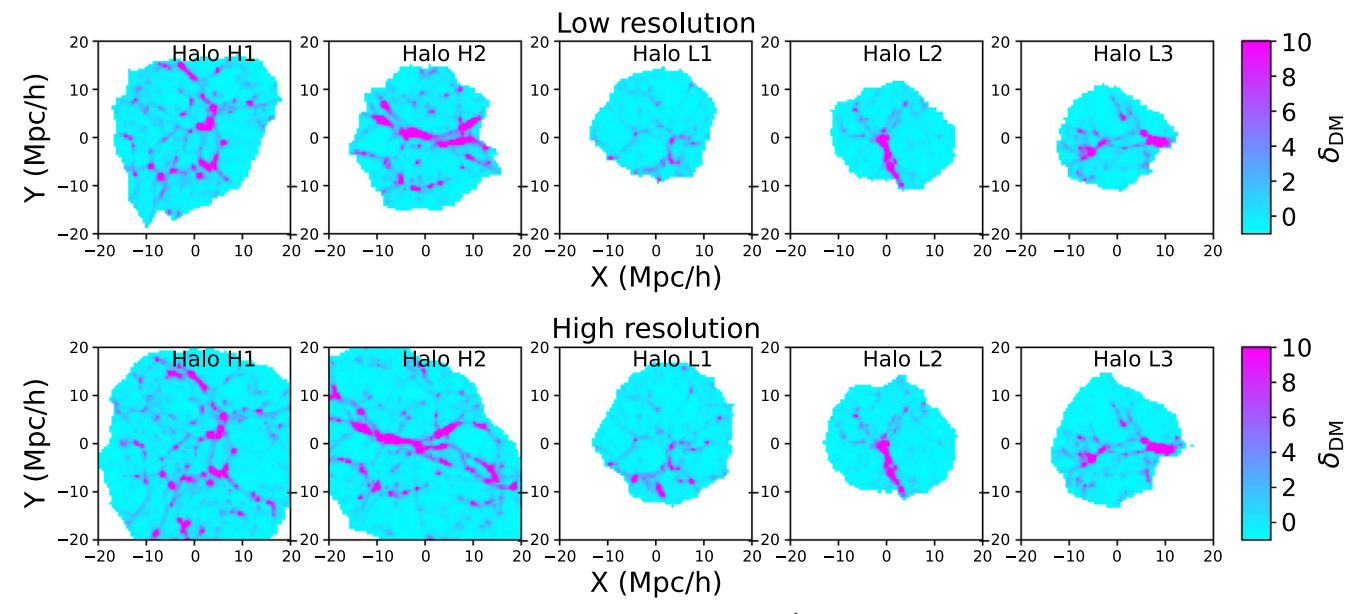


Figure 1. DM density fields of the protocluster zoom-in simulations in a slice of width $0.5 h^{-1}$ Mpc at z = 2. The clusters are ordered according to their z = 0 halo masses from highest on the left to lowest on the right. See Table 1 for the corresponding masses. The top row shows the low-resolution runs with the entropy-based preheating, whereas the bottom row shows the high-resolution ones with the energy-based preheating.

are at least "Virgo-like" ($M \gtrsim 4 \times 10^{14} \, h^{-1} \, M_{\odot}$), using the friends-of-friends (FoF) algorithm with a linking length of 0.2 in units of the mean interparticle separation. The FoF masses of the selected halos at z=0, 2, and 3 without preheating are given in Table 1. We note that preheating causes small changes in the measured masses of up to $\sim 1.5\%$ in the logarithm of the mass.

Second, we rerun the simulations with the selected clusters from z=127, including primordial gas for the halos using the zoom-in technique. An ellipsoidal region enclosing all DM particles within five times the virial radius at z=0 is resolved with higher resolutions, where a DM particle and a gas cell have mass resolutions of $m_{\rm DM}=1.6\times10^9$ and $m_{\rm g}=2.6\times10^8\,h^{-1}\,M_\odot$ in low-resolution runs (Section 2.2), and $m_{\rm DM}=2.0\times10^8$ and $m_{\rm g}=3.3\times10^7\,h^{-1}\,M_\odot$ in high-resolution runs (Section 2.3). These zoom-in runs are evolved with the Voronoi moving-mesh code AREPO (Springel 2010; Weinberger et al. 2020), where the mesh motions and adaptive mesh refinement maintain $m_{\rm gas}$ to be nearly constant within a factor of 2 while evolving the runs.

In order to focus solely on the effect of large-scale preheating on the protocluster gas, we turn off all feedback, as well as the formation of stars and black holes, magnetic fields, and metal cooling in these runs. We then inject energies into gas cells at z=3 according to two different preheating prescriptions that will be described in detail below. Since we are mainly interested in constraining the scale of the effect of preheating on the Ly α forest absorption, we adopt simple preheating prescriptions that only affect the thermal evolution of the gas, but do not have any detailed physical mechanism(s) behind them, such as the mechanical feedback due to AGN jets, which would require higher-resolution simulations to model accurately (see, e.g., Morganti 2017, and references therein).

In addition to the cluster simulations, we also performed the same type of simulations where we instead zoom into six randomly selected regions. These are cubic volumes with a comoving side length of $30 h^{-1}$ Mpc at the starting redshift z = 127. These regions combined are more representative for

the cosmic mean and were used for the normalization of the $Ly\alpha$ transmission. We note that in all cases we mask the regions filled with the high-resolution gas cells and only include those areas in our analysis, since the outer regions with the coarse gas cells are not resolved sufficiently and would mostly function as noise.

2.1. Extracting Mock Lyα Skewers

Mock Ly α skewers are generated for each simulation and at every snapshot along the z-axis with a resolution corresponding to $0.5 \, h^{-1}$ Mpc, or in velocity units, $\delta v = \frac{L}{h(1+2L)} \times H(z) / (1+z)$ km s⁻¹, with H the Hubble parameter and L the length of the simulation box. In this case, $L=300 \, h^{-1}$ Mpc. The term 2L corresponds to the number of pixels desired along the z-axis. We only extract skewers in the central $60 \times 60 \, h^{-1}$ Mpc in the x-y plane, encompassing the full zoomed-in region, and leave the rest of the box empty because those pixels are masked out for the final analysis.

The Ly α optical depths for all skewers are calculated using the FAKE_SPECTRA software package (Bird 2017). This PYTHON module is capable of handling the Voronoi kernel and is specifically designed to work on moving-mesh simulations with codes such as AREPO adopted here. Taking the H I fractions and temperatures directly from the data of gas cells, the FAKE_SPECTRA code generates Ly α optical depth convolved with the velocities including thermal broadening in any desired resolution along the specified line of sight.

All of the skewers are normalized to the mean $\text{Ly}\alpha$ transmission $\bar{F}(z)$ observed by Becker et al. (2013). The normalization constant for every redshift snapshot is determined from the combination of the simulations zooming into the random fields without preheating. As is common practice in the field, we work with the transmission overdensity defined as $\delta_F \equiv F/\bar{F}-1$. The final tomographic map is constructed by placing the skewers back into a three-dimensional grid.

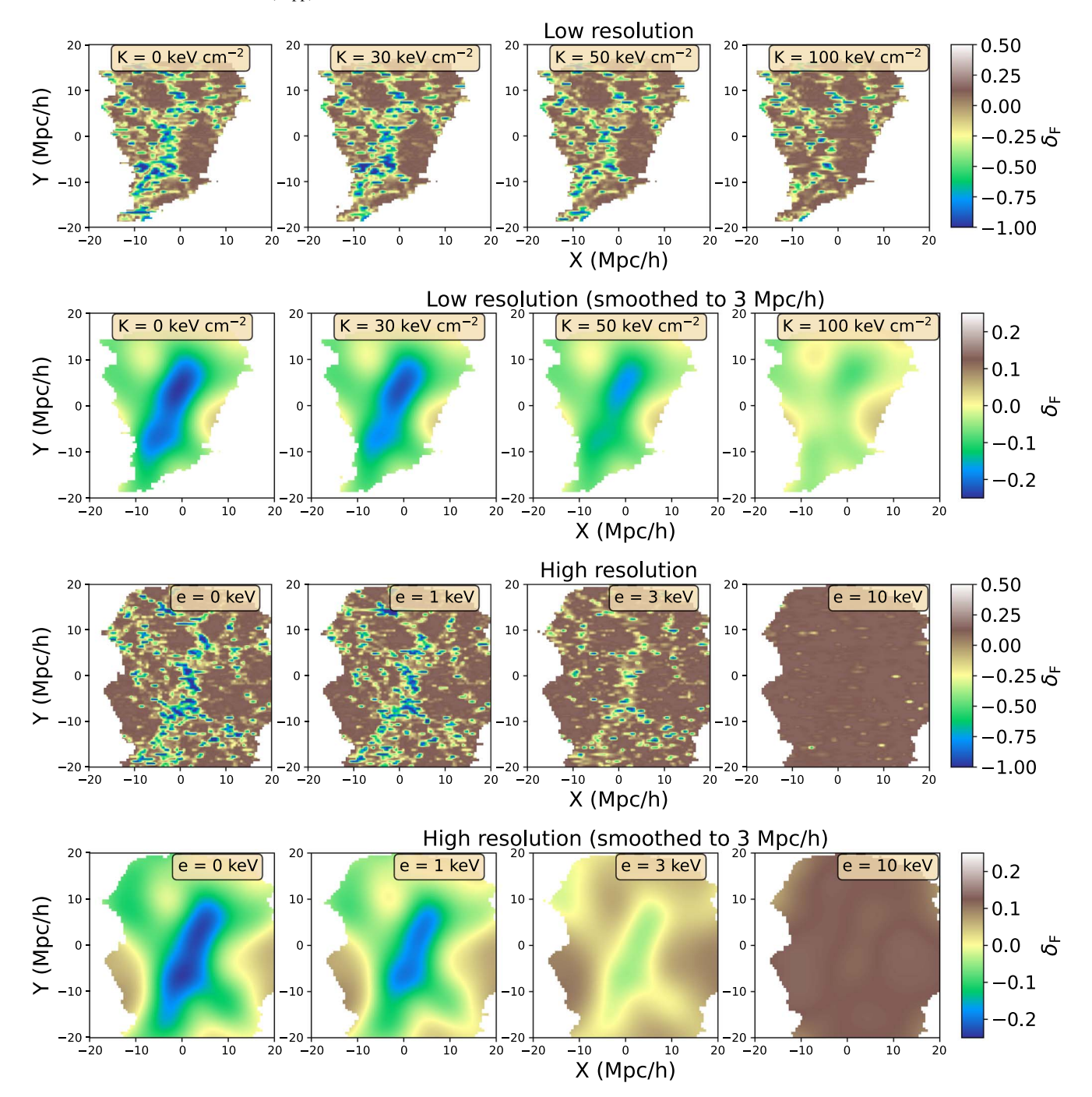


Figure 2. Ly α transmission maps of the protocluster in halo number H1 at z=2 for the different levels of the two preheating schemes. The floor levels increase from no energy injection (left) to maximum energy injection (right), where the top two rows show the low-resolution runs with entropy floors and the bottom two rows show the high-resolution simulations with energy floors. Both the raw maps and the maps smoothed with a Gaussian kernel of width 3 h^{-1} Mpc are shown. The latter smoothing scale is the same as that used to analyze the transmission relative to the underlying density field.

2.2. Low Resolution: Entropy Floor

The first set of simulations, hereafter referred to as "low resolution," has a mass resolution of $m_{\rm g}=2.6\times 10^8\,h^{-1}\,M_{\odot}$. For these runs, we implement preheating following the method developed by Borgani et al. (2001). Briefly, at z=3, we check the internal entropies of all cells with a gas overdensity $\delta_{\rm g}>5$, where internal entropy is defined as $K\equiv T\cdot n_{\rm e}^{-2/3}$, with $n_{\rm e}$ the electron number density and T the temperature of the cell. If the entropy is lower than a chosen value $K_{\rm floor}$, we increase the temperature of the gas cell to raise its entropy to this entropy floor. The gas is

then left to evolve as it normally would with the cooling effect. The above implementation implies that a denser gas cell with a higher $n_{\rm e}$ obtains a higher temperature by the preheating as $T=K_{\rm floor}\cdot n_{\rm e}^{2/3}$. Neither low-density gas with $\delta_{\rm g}<5$ nor hot gas whose entropy is originally above $K_{\rm floor}$ at z=3 are subject to the preheating. In this paper, we adopt values of $K_{\rm floor}=0$, 30, 50, and 100 keV cm² for the entropy floors, similar to those used in Borgani et al. (2001). The case of $K_{\rm floor}=0$ corresponds to the run without preheating. Much higher entropy floors with values of 300 keV cm² and above have already been ruled out from X-ray and Sunyaev–Zeldovich effect observations (Iqbal et al. 2017).

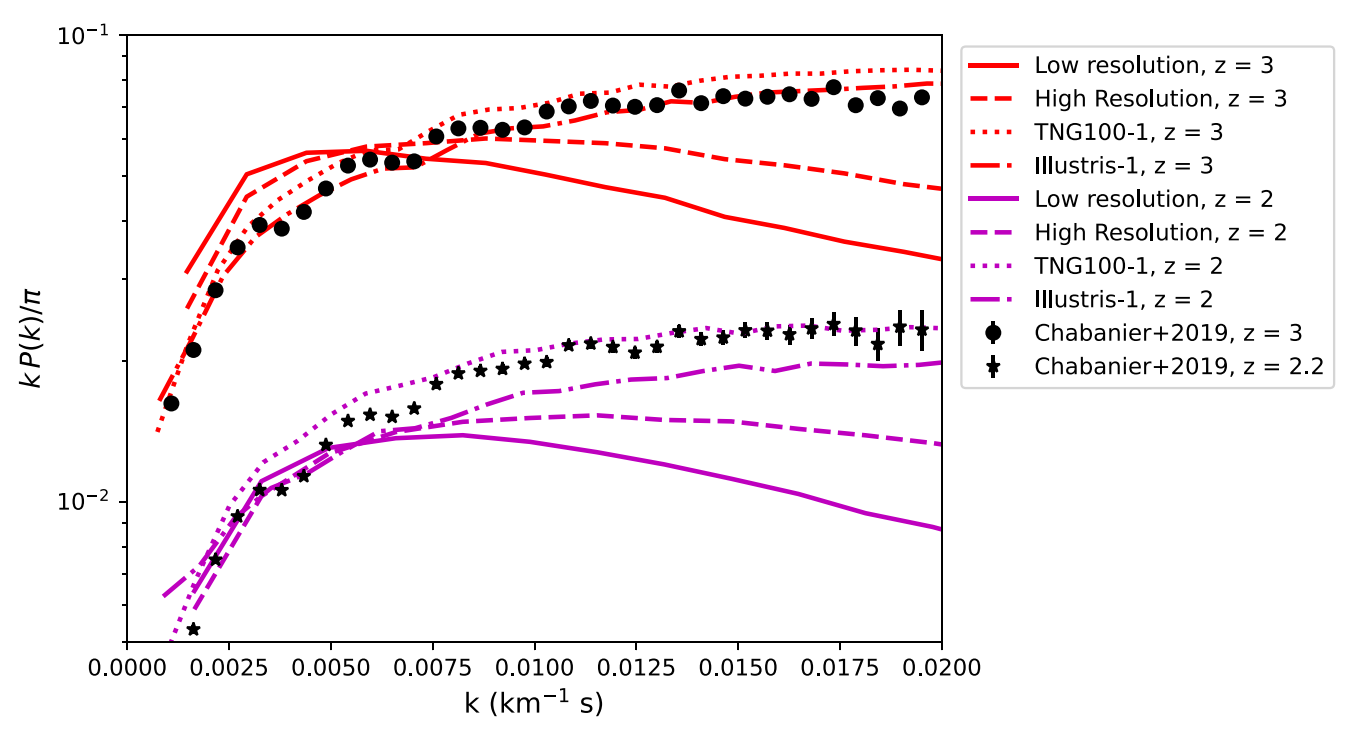


Figure 3. One-dimensional line power spectra of our simulations for the random fields with the low (solid lines) and high resolutions (dashed lines). The power spectra at z=3 are denoted in red and z=2 in magenta. For comparison, we also show the SDSS DR14 data (Chabanier et al. 2019) at z=3 (black dots) and z=2.2 (black stars), as well as the Illustris-1 (dashed–dotted lines) and TNG100-1 (dotted lines) simulations at z=2 and 3. The black stars at z=2.2 have been downscaled by a factor 1.7 to more easily compare with the z=2 simulations. In both cases, the low-resolution simulations lack significantly more power at scales smaller than $k \ge 0.01$ km⁻¹ s than the high-resolution ones.

This simple preheating prescription has the benefit that it does not make assumptions about the underlying physical mechanism(s) that drive(s) the preheating, allowing for constraints on the total nongravitational energy deposited into the ICM through the preheating. Once a detection can be made, more detailed modeling can then be performed in order to work out what the exact origin of the preheating is. In the top row of Figure 1, we show a slice of the real-space DM density field at z=2 for each of the protoclusters in the low-resolution simulations over a $0.5 \, h^{-1} \, \mathrm{Mpc}$ width. Moreover, the effect of this preheating scheme on one of the halos can be seen in the Ly α transmission maps in the top two rows of Figure 2. The higher the level of the entropy floor, the smaller the regions with strong absorption become.

We note that the resolution of these simulations does not recover the full range of scales that can be probed with the current generation of Ly α forest observations. This can be seen clearly in the one-dimensional line power spectrum obtained from the combination of the simulations for the random fields shown in Figure 3. Both at z = 3 and 2, the power spectrum of these simulations (dashed red and magenta lines, respectively) cuts off strongly at scales smaller than $k \gtrsim 0.01 \text{ km}^{-1} \text{ s}$ compared to either Data Release 14 of the Sloan Digital Sky Survey (SDSS DR14; Chabanier et al. 2019) or the Illustris-1 (Vogelsberger et al. 2014a, 2014b; Nelson et al. 2015) and IllustrisTNG (TNG100-1; Nelson et al. 2019) simulations. Mock Ly α skewers for the latter two were created following the same methodology applied to the protocluster simulations, as described in Section 2.1. However, at $k \lesssim 0.01 \, \mathrm{km^{-1}} \, \mathrm{s}$ (corresponding to scales of larger than several hundred $\mathrm{km^{-1}} \, \mathrm{s}$ or several megaparsecs), the power spectrum matches adequately to allow our subsequent analysis of the smoothed transmission field.

2.3. High Resolution: Energy Injection

In order to improve upon the recovery of the 1D line power spectrum, we additionally run a set of the high-resolution simulations with the mass resolution of $m_{\rm g}=3.3\times 10^7\,h^{-1}\,M_{\odot}$. This is similar to the low-resolution run of the IllustrisTNG simulations (TNG100-3) and performs better at recovering the observed Ly α forest scales (see Figure 3). We note that even these higher-resolution simulations lack power at small scales. However, since we eventually smooth all our maps to scales of $3\,h^{-1}$ Mpc, it should not significantly affect our results.

Another issue is that, at these high resolutions, the preheating scheme using the entropy floors described in Section 2.2 breaks down, since some of the gas cells around the cluster centers can achieve quite high densities. Therefore, the entropy-based preheating increases their temperatures to extraordinary values, resulting in clusters that explode soon after the heat injection and completely dissipate the gas in the protocluster region. Due to the increased resolution and the exclusion of the formation and feedback of stars and black holes, there are many more of these high-density cells inside the same small volume than there were in the low-resolution runs, causing the thermal runaway.

Instead of the entropy-based preheating, we therefore adopt a different preheating scheme for the high-resolution runs, where we increase the specific energies of all gas cells to a constant floor value independent of density. We adopt energy floors of $e_{\rm floor}=0$, 1, 3, and 10 keV for these high-resolution runs. If the internal energy of a gas cell is below $e_{\rm floor}$, its temperature is increased to the floor value at redshift z=3, irrespective of its overdensity $\delta_{\rm g}$. In this case, the temperature of all gas cells in the clusters will thus be lifted to the same value. The resulting Ly α transmission will then mostly depend on the gas density. The floor values of this preheating scheme are motivated by the observed nongravitational

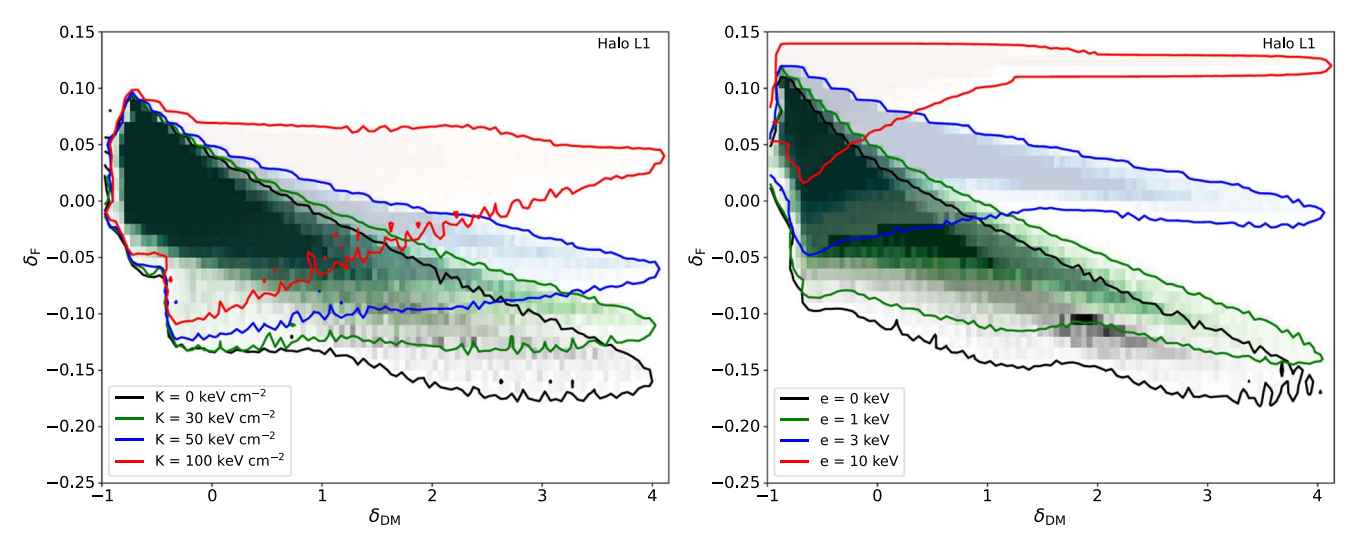


Figure 4. Ly α transmission—DM density distribution of the protocluster in halo number L1 (see Table 1) at z=2. On the left we show the low-resolution simulations with entropy-based preheating scheme (Section 2.2), and on the right side the high-resolution runs with energy-based preheating are presented (Section 2.3). Both fields have been smoothed with a Gaussian kernel of 3 h^{-1} Mpc. The contours show the 2% level of the PDF of the distribution. The more the ICM is preheated, the more the distribution tilts toward higher transmission at the high DM density side.

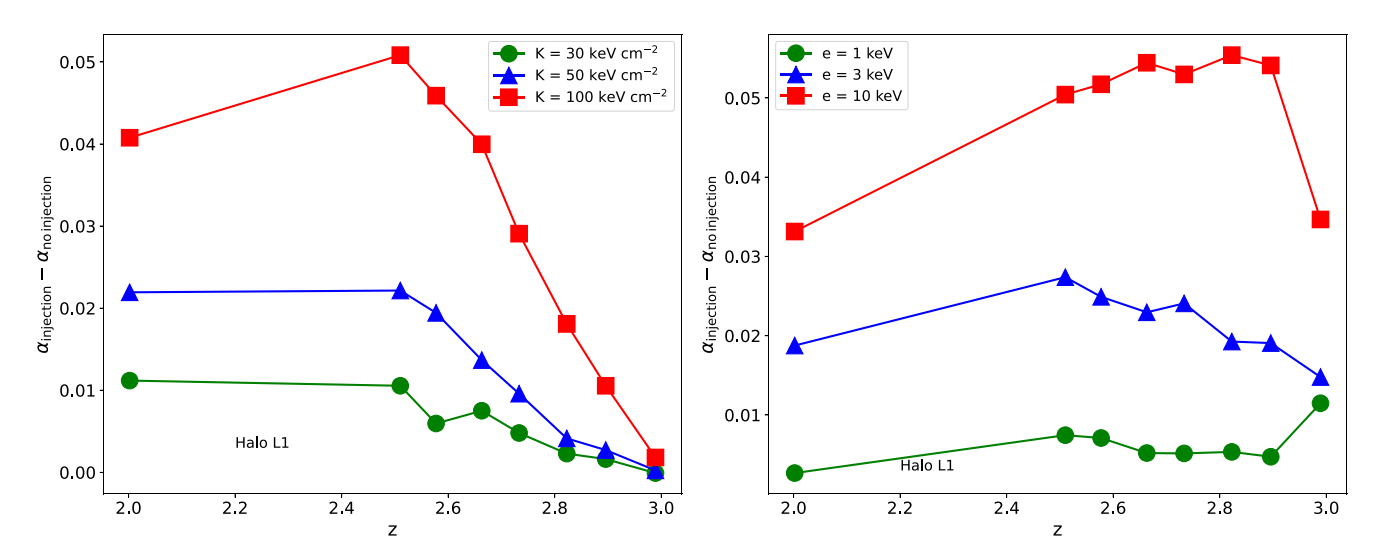


Figure 5. Redshift evolution of the difference in slope between the Ly α transmission—DM density distribution with and without preheating for the protocluster in halo L1. Slopes are measured from the distribution at smoothed DM densities $1 \le \delta_{\text{DM}} \le 3$. The left panel shows the low-resolution simulation with an entropy floor based preheating scheme and the right panel shows the high-resolution run with energy-based preheating.

energy in clusters, where central AGNs have been measured to be able to inject several keV of energy into the central ICM (e.g., Chaudhuri et al. 2013). The DM density fields of these highresolution simulations are given in the bottom row of Figure 1. The regions filled with the high-resolution gas cells have become larger in the two most massive clusters compared to their lowresolution counterparts in Section 2.2. How this energy floor based preheating scheme affects the Ly α transmission of one of the protoclusters at z=2 is shown in the two bottom rows of Figure 2. We also note that the heating in the simulations with $e_{\rm floor} = 10 \,\mathrm{keV}$ is unrealistically high and indeed almost all of the HI gas has been ionized inside the entire protocluster region (see bottom right image in Figure 2). It therefore mainly serves as an extreme upper limit to eventually help put constraints on real data. It is also worth noting that the volume fraction of our simulation occupied by progenitor particles of clusters with $M(z=0) \gtrsim 4 \times$ $10^{14} h^{-1} M_{\odot}$ is only $\sim 0.2\% - 0.8\%$ at z = 2 and $\sim 0.3\% - 1\%$ at

z=3. Therefore, even such an extreme level of energy injection might not be detectable in analyses of global Ly α forest statistics in the current generation of observational quasar surveys, if they were confined to protocluster regions of massive clusters.

3. Results and Discussion

By combining the DM density field with the $Ly\alpha$ absorption field, it becomes possible to distinguish regions of the protoclusters in which the effect of preheating is most prevalent. The distribution of these two quantities thus makes up the main tool for our analysis in this work. The DM density fields have been convolved with the z-axis velocity fields to convert them to redshift space, which tightens the relation with the line-of-sight $Ly\alpha$ absorption, since the latter is also observed in redshift space. Both the $Ly\alpha$ absorption field and the redshift-space DM density field are then smoothed with a

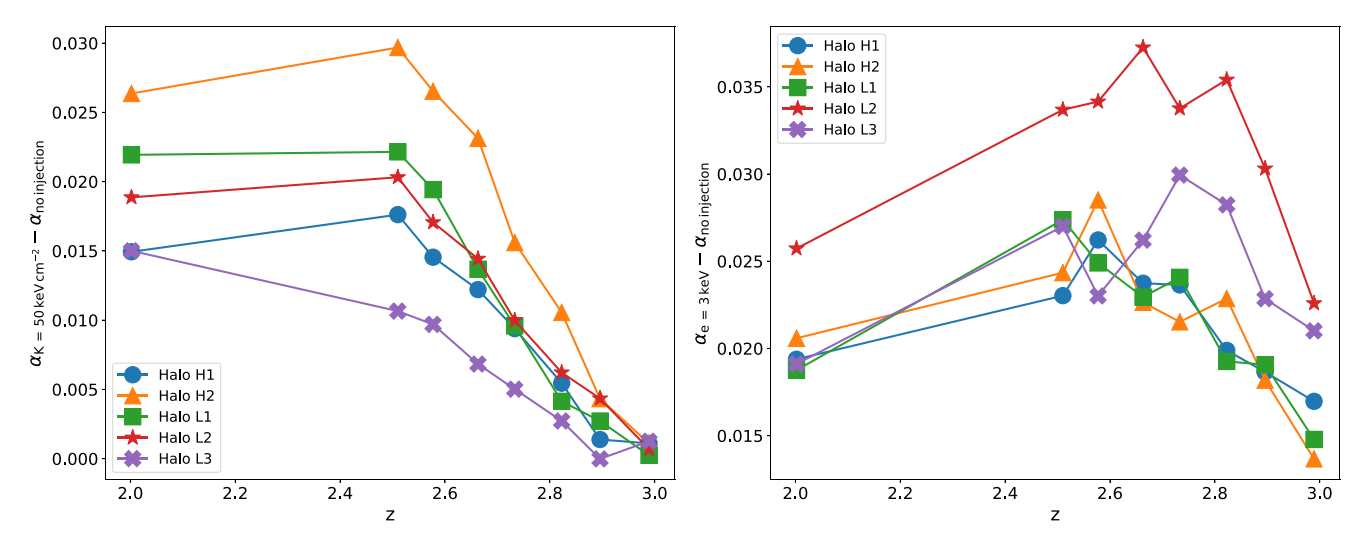


Figure 6. Redshift evolution of the difference in slope between the Ly α transmission—DM density distribution with and without the intermediate level preheating for all of the simulated protoclusters. The left panel shows the results for the low-resolution simulation with a $K_{floor} = 50 \text{ keV cm}^{-2}$, whereas the panel on the right shows the high-resolution simulation results with E = 3 keV energy injection. The labels in the legend are ordered by decreasing z = 0 mass, the values of which can be found in Table 1. All slopes were derived from the distribution at smoothed DM densities $1 \le \delta_{\text{DM}} \le 3$.

Gaussian kernel of standard deviation $\sigma = 3 h^{-1}$ Mpc. This is the same smoothing scale shown in several panels of Figure 2.

3.1. Transmission—Density Distribution

The resulting transmission—density distribution for the intermediate-mass protocluster in halo L1 at redshift z=2 is shown in Figure 4, where the left panel represents the low-resolution run with an entropy floor, and the right panel the high-resolution simulation with the energy floor based preheating. The same plots for the other protoclusters, as well as the results for z=2.5 and 3, are shown in Appendix A. In all cases, the contours denote the 2% level of the PDF of the distribution. For comparison, we also show the transmission—density distributions from the combined "random" zoom-in simulations that do not represent particularly over- or underdense regions in Appendix A. As expected, these random fields contain far fewer overdense particles ($\delta_{\rm DM} \gtrsim 1.5$) than the protocluster regions.

As can be seen in these distributions, the entropy-based preheating scheme adopted in the low-resolution runs causes the transmission—density distribution at z=2 to tilt upwards toward higher transmission at high matter density. At the low-matter density side of the distribution, there is only a small effect, which indicates that the entropy floor is in practice mostly applicable to overdense gas cells in the simulations. Another point to note is that there appears to be an evolution with redshift in the slope of the transmission—density distribution, as there is almost no difference between the different energy injection levels right after the energy injection at z=3 (see Figure 8) despite the large differences at z=2. This will be discussed in more detail in Section 3.2 below.

In the high-resolution runs with the energy-based preheating, the lower bounds at the low-matter density side of the distribution do get lifted up toward higher transmission, which is a consequence of energy being injected to all particles at the injection redshift regardless of overdensity. Since the low-matter density regions originally already had high ${\rm Ly}\alpha$ transmission before the energy injection and due to the exponential nature of the transmission, the effect of the internal energy floor on the

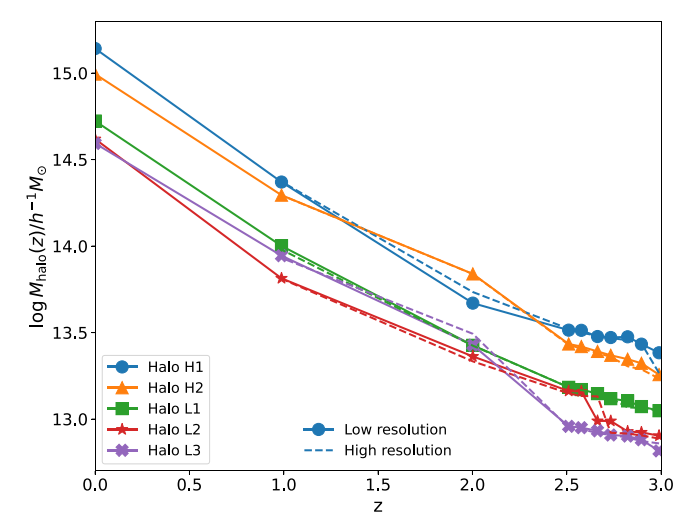


Figure 7. Evolution of the halo mass with redshift of the five simulated clusters. The solid lines denote the FoF masses of the low-resolution runs and the dashed lines show the high-resolution results.

transmission remains stronger for the high-density regions. This results in a similar behavior for the contours as in the low-resolution simulations, except for z=3, where there now is a clearer difference between the different levels of energy injection (see Figure 11). As mentioned before, at the extreme energy injection level of $e_{\text{floor}}=10\,\text{keV}$, most of the H I gas has been ionized at all densities, resulting in an almost flat transmission —density distribution.

3.2. Effects on the Transmission-Density Slope

Coming back to the apparent evolution of the slope of the transmission—density distribution with redshift, this section discusses the effect of preheating on the slope in more detail. Although the whole distribution could be represented by a power law, since the effect of the preheating mainly manifests itself at high density, we focus the remainder of the discussion on that side of the distribution. We therefore evaluate the slope in the range $1\leqslant \delta_{DM}\leqslant 3$ of the smoothed DM density field by

fitting a linear relation for every output snapshot of each of the simulated protoclusters. In order to quantify the effect of the preheating, we then subtract the slope of the distribution without the injection $\alpha_{\rm no~injection}$ from the slope with heat injection $\alpha_{\rm injection}$ and plot this slope difference as a function of redshift for the intermediate-mass protocluster L1 in Figure 5.

In both types of simulations, it is clear that across the entire redshift range, the stronger the energy injection is, the larger the difference in slope becomes. For the halo L1 protocluster in the low-resolution case, the slope difference starts out small immediately after the preheating and increases with time at least until $z \sim 2.5$. This signifies that the preheating gets processed by the gas in the clusters and, as the high-density regions accrete more matter, they grow denser and accumulate more of the heated gas, which tilts the transmission-density distribution further upwards. After z = 2.5, the normal cooling processes take over and again drive the high-density tail of the distribution down, either flattening the curve or driving it back down slightly toward z = 2. For the lowest entropy floor level of $K_{\text{floor}} = 30 \text{ keV cm}^{-2}$, the evolution remains roughly flat, signifying that the regular gravitational processes governing the evolution of the gas in the ICM dominate and cause the heated gas to spread out more evenly. This leaves the slope difference roughly constant over the considered redshift range. In the high-resolution simulations with energy floors, the evolution in general is more flat due to all cells being heated to roughly the same temperature at the time of injection. The same figures for the other protoclusters are shown in Figures 14 and 15 in Appendix B and indicate that they all mostly follow the same trends as the intermediate-mass halo L1. We note that for lower-mass clusters, the high-resolution zoom-in region is smaller and they have not reached very high densities by $z \sim 3$, resulting in noisier transmission-density contours, which consequently makes the measured slopes less reliable.

To investigate whether there is a trend in mass for the redshift evolution, we additionally show the same evolution for all of the halos together, but at a single level of preheating (i.e., $K_{\rm floor} = 50~{\rm keV~cm^{-2}}$ for the low-resolution runs and $e_{\rm floor} = 3~{\rm keV}$ for the high-resolution ones) in Figure 6. The same figure for the other values of the entropy- and energy-based injections are again shown in Appendix B in Figure 16. Moreover, the evolution of the central halo masses with redshift is shown in Figure 7.

Despite there being a clear separation between the mass evolution of the high-mass clusters (H1 and H2) and the lowermass ones (L1, L2, and L3) in Figure 7, this is not reflected in the evolution of the slope differences and there does not appear to be a trend with the halo mass of the cluster. The magnitude of the slope difference, in general, is very similar the across the different protoclusters in Figure 6, with the differences all lying within a factor of \sim 2. Nonetheless, the higher-resolution simulations with energy floors do appear to be more strongly influenced by the formation history of the protocluster. For the protoclusters in halos L2 and L3, the mass buildup between redshift \sim 2–3 varies more rapidly than for the other clusters, also resulting in stronger fluctuations in the evolution of the slope difference. This indicates that the additional gravitational shock heating caused by big mergers in these protoclusters overwhelms the effect of preheating. Given the small sample studied in this work, this would have to be investigated in more detail in a future study. Moreover, at the lower levels of entropy and energy injection, the curves fluctuate more strongly than for the higher levels of injection. This

further suggests that the preheating in these cases is not always the dominant source of heating governing the evolution of the ICM gas.

3.3. Prospects for Detecting Preheating in Observations

From the results presented above, it is clear that the strength of the constraints on preheating from any Ly α forest tomographic survey depends on redshift. Although the preheating affects the gas at all densities (especially in the high-resolution simulations), in general it takes time for the heating in the gas to be processed and manifest an effect on the transmission—density relationship. Directly after the injection of the energy (typically predicted to occur at $z \sim 3$), the difference is smallest. Hence, in order to put the strongest constraints on the preheating magnitude, the suitable redshift range to target with observations would be $2 \le z \le 2.7$.

A survey that will be ideally suited for such a study is CLAMATO (Lee et al. 2018). This Ly α forest tomographic survey covers the central part of the COSMOS field with a mean sightline separation of $2.4 \, h^{-1}$ Mpc, comparable to the smoothing scales adopted in this study, and probes a sizeable volume of $\sim (75 h^{-1} \text{Mpc})^3$ in the redshift range $2.05 \leqslant z \leqslant 2.55$. Moreover, it has been shown to encompass a number of galaxy protoclusters, such as the massive Hyperion protocluster at z=2.45 (Lee et al. 2016; Wang et al. 2016; Cucciati et al. 2018), as well as a protocluster discovered in the z-FOURGE galaxy survey at z=2.1 (Spitler et al. 2012; Nanayakkara et al. 2016).

Recently, Ata et al. (2021) produced a Bayesian reconstructed DM density field covering the same region of the COSMOS field by combining data from multiple spectroscopic redshift surveys. This enables us to study in detail the formation and evolution of these aforementioned protoclusters (M. Ata et al. 2022, in preparation). Furthermore, the combination of the CLAMATO data set with such a reconstruction would provide the data required to perform the preheating analysis proposed in this work for the protoclusters within the field. If any protoclusters are found that display transmission—density relations characteristic of preheating as shown in this paper, then follow-up observations to search for radio galaxies or AGNs within these regions could help identify the mechanisms that drive cluster preheating.

In 2023, the Prime Focus Spectograph (PFS) will come online on the Subaru Telescope and will dramatically increase the field of view (1.25 deg²) and multiplex (2400 fibers) available on 8 m class telescopes. As part of the Galaxy Evolution Survey being planned by the PFS collaboration, there will be a Ly α tomography component that will cover $\sim 12 \, \text{deg}^2$ over the redshift range 2.3 < z < 2.7. This will sample a large number of background sightlines at similar area densities as CLAMATO and LATIS, while representing a $\sim 40 \times$ and $\sim 7 \times$ increase in total volume, respectively, compared to both current surveys. Simultaneously with the Ly α tomography survey, a sample of coeval foreground galaxies will be observed within the 2.3 < z < 2.7 redshift range probed by the Ly α forest, for the purpose of being compared with the Ly α forest absorption (see the Appendix of Nagamine et al. 2021 for an overview). At a number density $n \sim 1.2 \times$ $10^{-3} h^3 \,\mathrm{Mpc}^{-3}$, this is roughly equivalent to the combined galaxy redshift sample used by Ata et al. (2021) and will allow for highquality density reconstructions. With approximately $\sim 300-500$ galaxy protoclusters with $M(z=0) \gtrsim 4 \times 10^{14} h^{-1} M_{\odot}$ expected to be detected within the survey volume, the PFS Galaxy Evolution Survey will enable statistical studies of cluster preheating and its potential sources.

4. Conclusions

The existence and cause of preheating in galaxy clusters remain open questions. In this work, we propose a method to use Ly α forest tomographic maps, combined with reconstructions of the underlying DM density field, to detect signs of preheating as well as put constraints on the magnitude of the energy injected into the ICM at Cosmic Noon ($z \sim 2.5$). We adopt two sets of cosmological zoom-in simulations for galaxy clusters and consider different implementations of the preheating for the gas at the redshift z=3. We compute Ly α tomographic maps in the range $2 \leqslant z \leqslant 3$. In the first suite of five protoclusters, our preheating scheme injects thermal energy into the high-density gas according to fixed entropy floors. For the second set of runs, using the same initial conditions, preheating is implemented by imposing fixed energy floors on all gas cells.

We find that the preheating affects the slope of the Ly α transmission-DM density distribution, where the stronger the preheating that is applied, the more the distribution tilts toward higher transmission. Furthermore, the differences in these slopes between simulations with and without preheating show an evolution with redshift. The difference in general is smallest just after the energy injection at z = 3, but it evolves toward a peak at $z \sim 2.4-2.6$ and then flattens out or becomes smaller toward z = 2. We additionally find that the energy floor based preheating scheme adopted here is already prevalent immediately at z = 3, whereas the effect takes more time to appear for the entropy floor based preheating adopted in this work. Recent Ly α tomographic surveys for which information about the DM density field is also available, such as CLAMATO, will provide the ideal testbed for such a study. Being able to study multiple protoclusters in these large surveys will allow for putting constraints on the magnitude of the preheating, which in turn will help to distinguish between different models of galaxy and AGN feedback in galaxy clusters.

If the peak of nongravitational heating should be detected, it would shed light on the physical sources involved, which we have tentatively refrained from specifying, given the uncertainties. However, if the peak turns out to be in the neighborhood of z=2-3, it would be strongly suggestive that some form of AGN feedback may be responsible.

Moving beyond protoclusters, in a companion paper (Kooistra et al. 2022), we will also study the use of the $Ly\alpha$ forest transmission—density relationship in similar data sets to constrain the global fluctuating Gunn—Peterson relationship at Cosmic Noon.

The authors would like to express their gratitude to Joe Hennawi, Davide Martizzi, Daniele Sorini, Metin Ata, Ilya Khrykin, and Ben Horowitz for their invaluable discussion and technical support, as well as Volker Springel for kindly providing the simulation code AREPO. This study was supported by the World Premier International Research Center Initiative (WPI), MEXT, Japan. K.G.L. acknowledges support from JSPS Kakenhi grant Nos. JP18H05868 and JP19K14755. R.C. gratefully acknowledges support of NSF grant No. AST2007390. The simulations presented in this paper were carried out on the Cray XC50 at the enter for Computational Astrophysics, National Astronomical Observatory of Japan.

Appendix A Transmission—Density Distributions

In this Appendix we provide the $Ly\alpha$ transmission—DM density distributions of all of the halos not included in the main figures, as well as at three different redshift bins. The distributions for the low-resolution simulations with entropy floors are shown in Figures 8, 9 and 10, and those for the high-resolution simulations with energy floors can be found in Figures 11, 12 and 13.

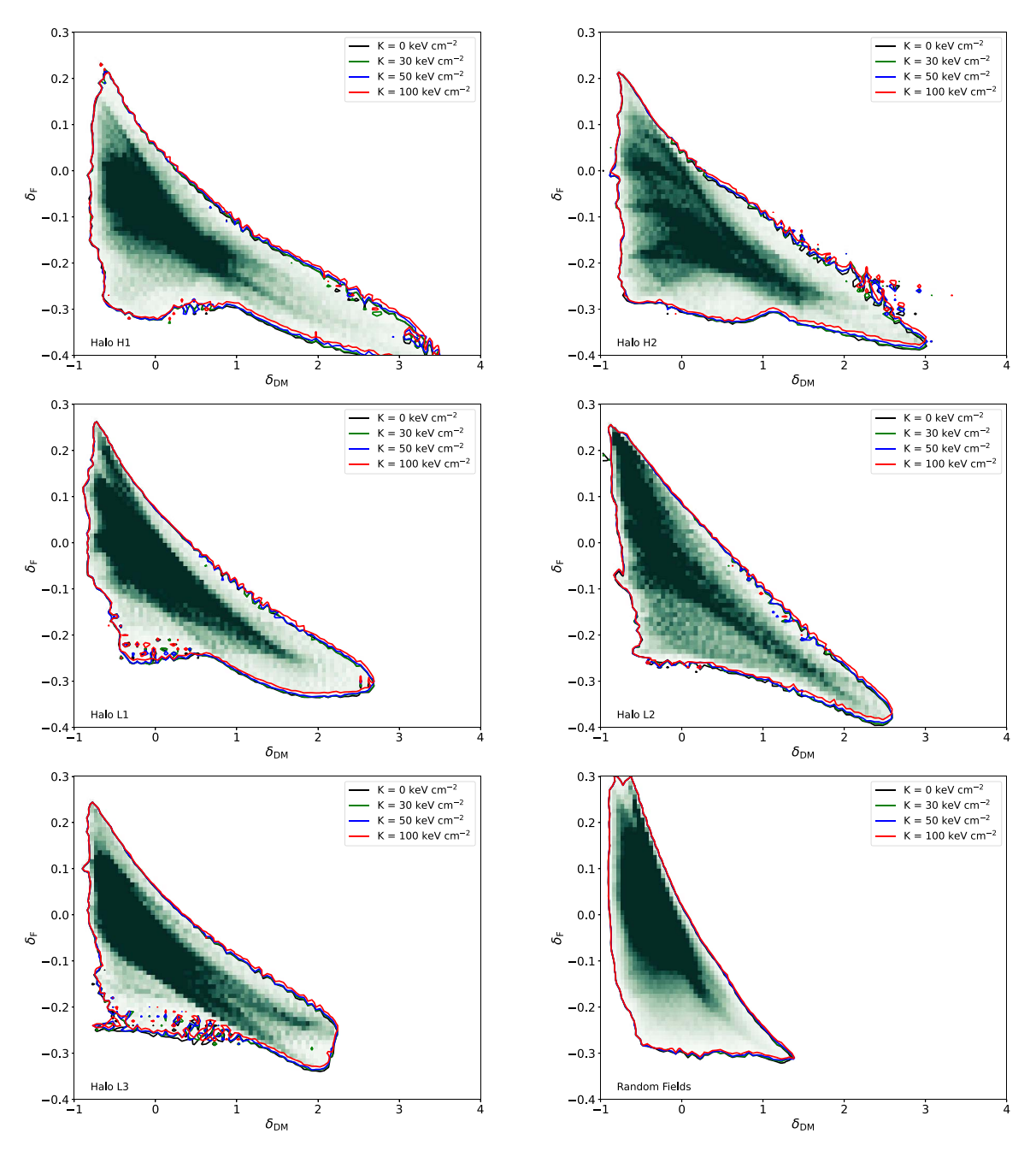


Figure 8. Ly α transmission—DM density distribution of all protoclusters (see Table 1) at z=3 in the low-resolution simulations with the entropy floors. The contours denote where the PDF of the distribution reaches the 2% level. The panels from left to right and top to bottom show the results of halos H1, H2, L1, L2, and L3, and a combination of six random fields, respectively (see Table 1).

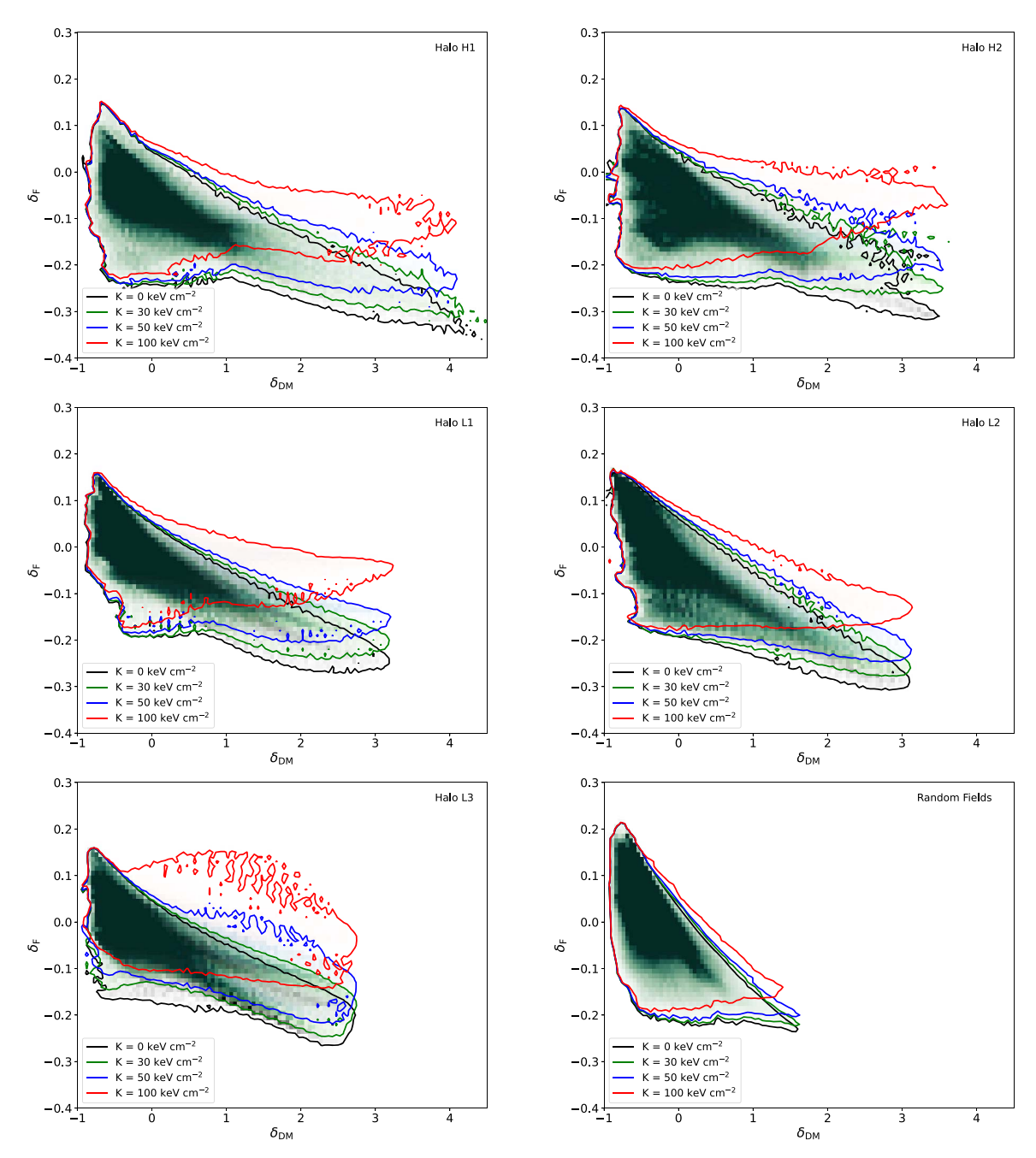


Figure 9. Ly α transmission—DM density distribution of all protoclusters at z=2.5 in the low-resolution simulations with the entropy floors. The contours denote where the PDF of the distribution reaches the 2% level. The panels from left to right and top to bottom show the results of halos H1, H2, L1, L2, and L3, and a combination of six random fields, respectively (see Table 1).

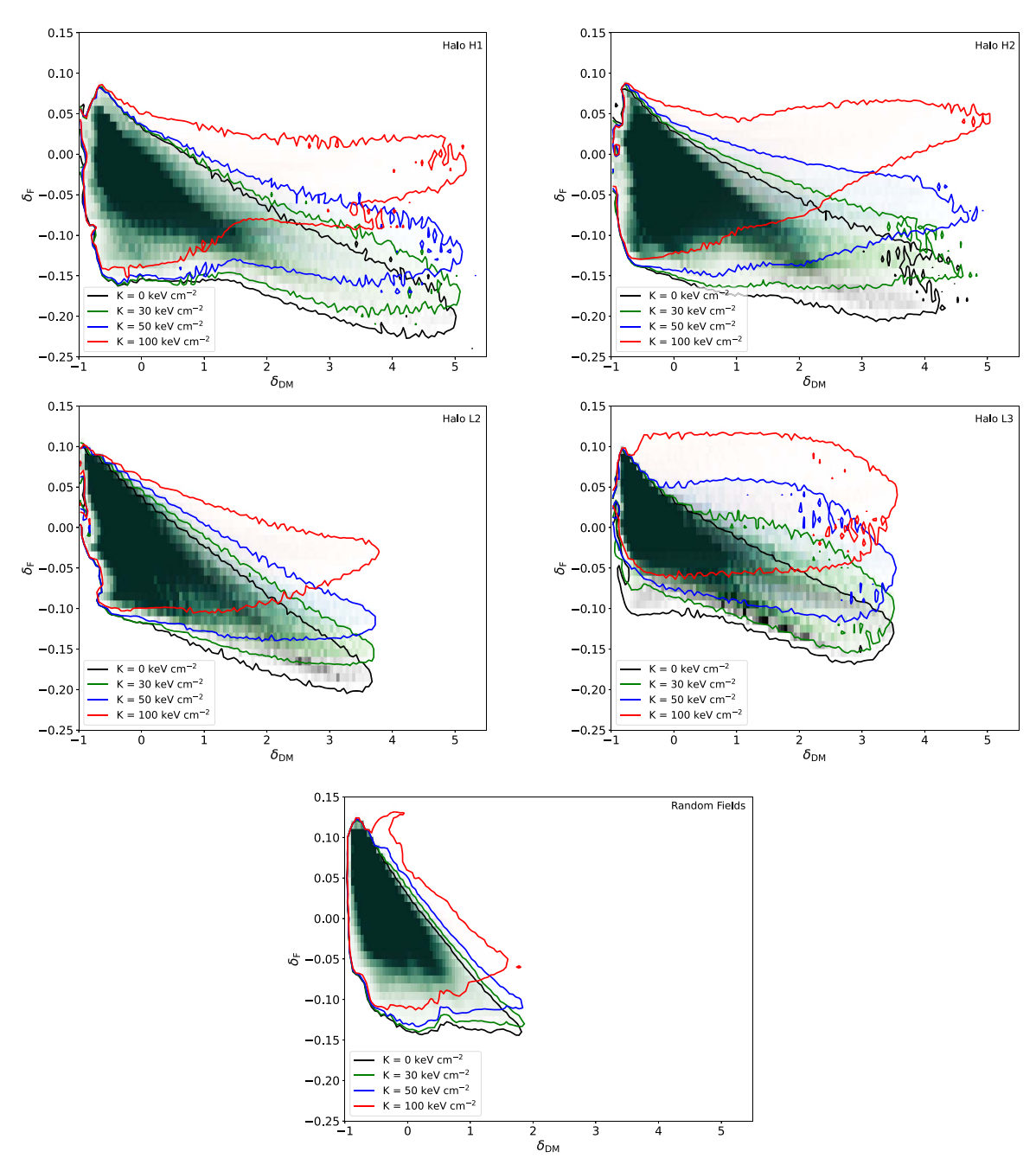


Figure 10. Ly α transmission—DM density distribution of the remaining protoclusters at z=2 in the low-resolution simulations with the entropy floors. The contours denote where the PDF of the distribution reaches the 2% level. The panels from left to right and top to bottom show the results of halos H1, H2, L2, and L3, and a combination of six random fields, respectively (see Table 1).

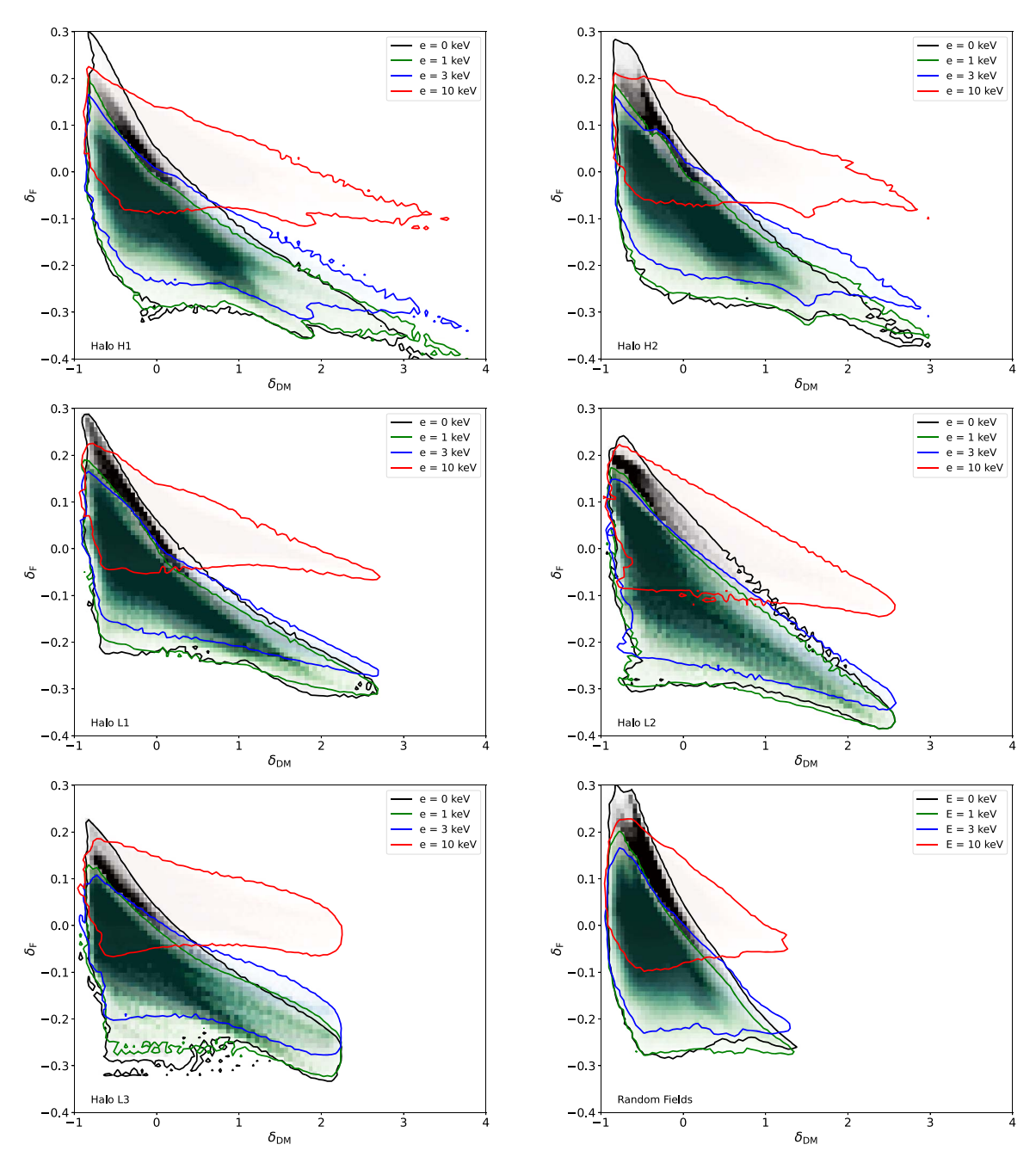


Figure 11. Ly α transmission—DM density distribution of all protoclusters at z=3 in the high-resolution simulations with the energy floors. The contours denote where the PDF of the distribution reaches the 2% level. The panels from left to right and top to bottom show the results of halos H1, H2, L1, L2, and L3, and a combination of six random fields, respectively (see Table 1).

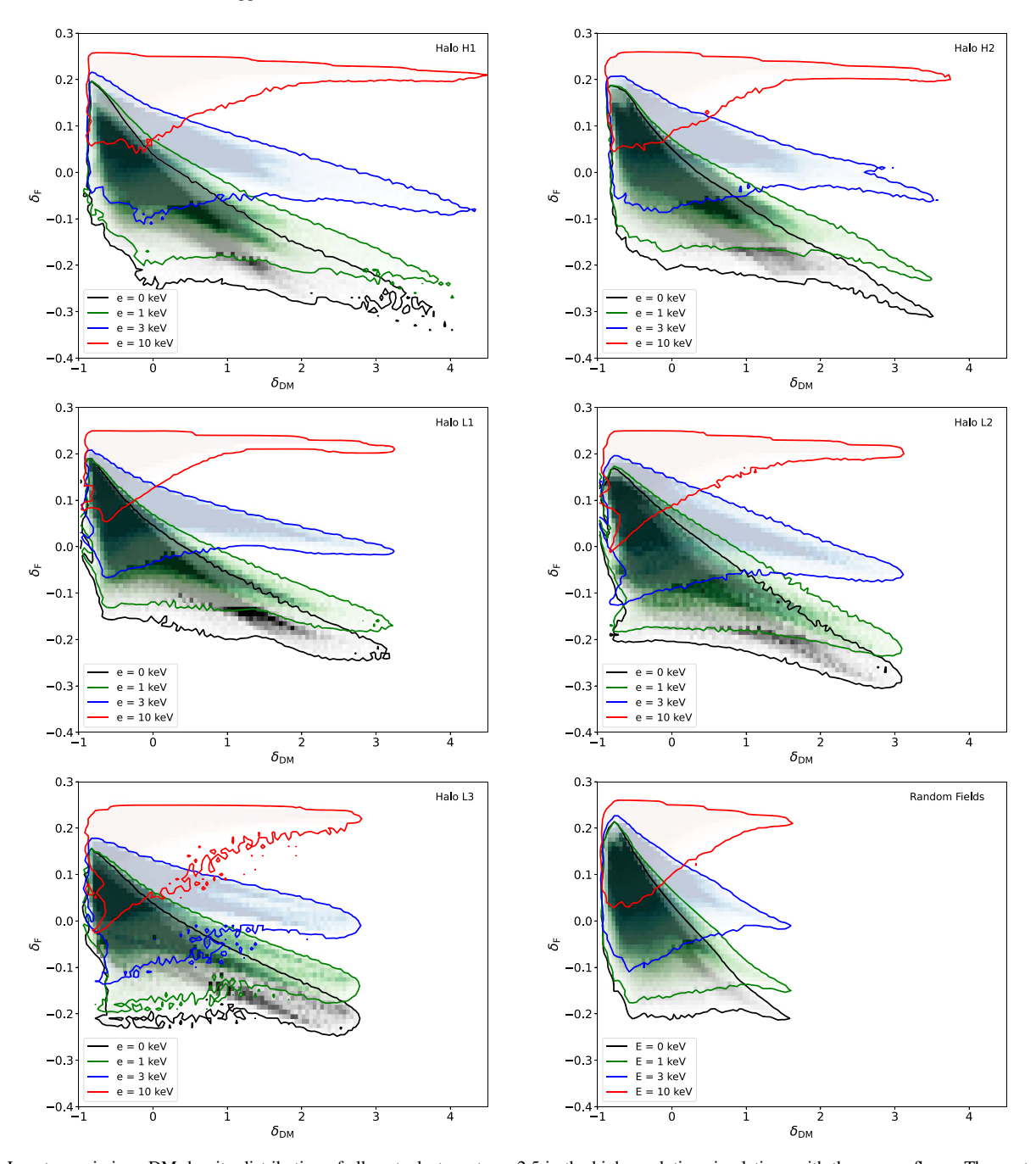


Figure 12. Ly α transmission—DM density distribution of all protoclusters at z=2.5 in the high-resolution simulations with the energy floors. The contours denote where the PDF of the distribution reaches the 2% level. The panels from left to right and top to bottom show the results of halos H1, H2, L1, L2, and L3, and a combination of six random fields, respectively (see Table 1).

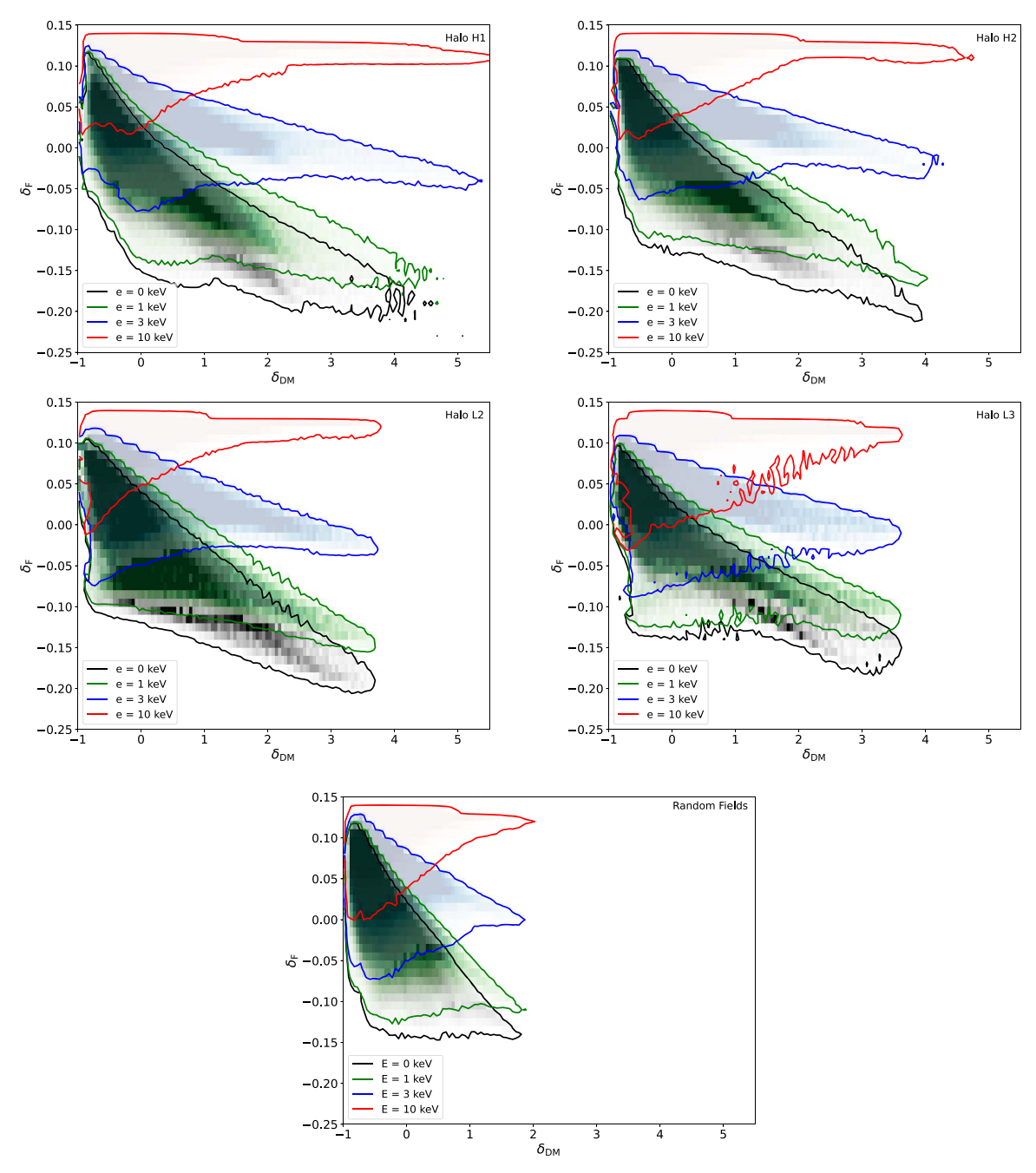


Figure 13. Ly α transmission—DM density distribution of all protoclusters at z=2 in the high-resolution simulations with the energy floors. The contours denote where the PDF of the distribution reaches the 2% level. The panels from left to right and top to bottom show the results of halos H1, H2, L2, and L3, and a combination of six random fields, respectively (see Table 1).

Appendix B The Redshift Evolution of the Slope Differences

The following figures illustrate the redshift evolution of the difference in slope of the Ly α transmission—DM density distribution that were not included in the main text of the paper. The difference in slope of the individual low-resolution

simulations can be found in Figure 14. The same for the high-resolution simulations is given in Figure 15. The plots of the differences in slope of all simulations per entropy or energy floor level are shown in Figure 16.

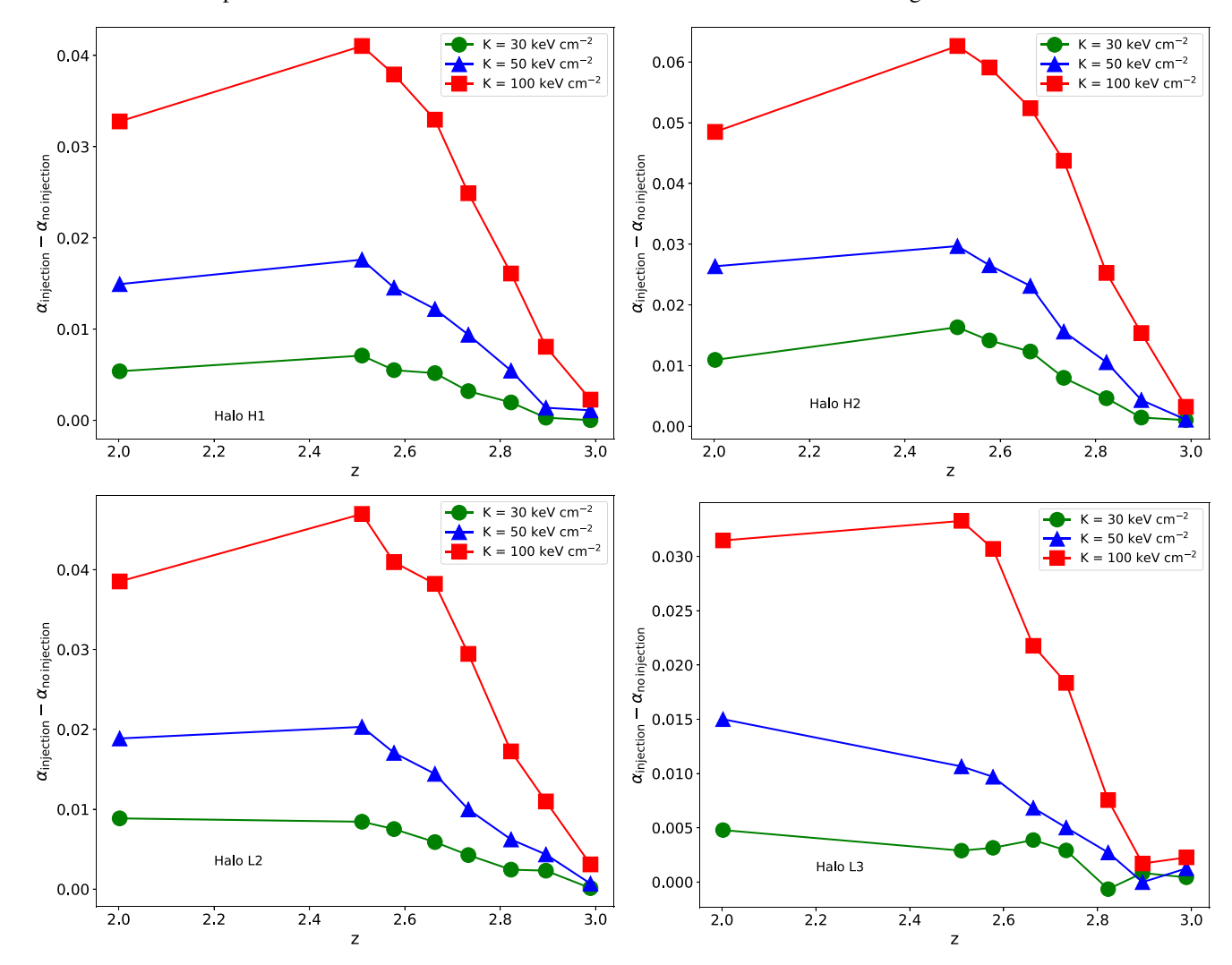


Figure 14. The redshift evolution of the difference in slope between the Ly α transmission—DM density distribution with and without preheating for the protocluster in the remaining halos in the low-resolution simulations with the entropy floors. The slopes are measured at the high-density side of the distribution with smoothed DM densities $1 \leqslant \delta_{\rm DM} \leqslant 3$. The panels from left to right and top to bottom show the results of halos H1, H2, L2, and L3, respectively.

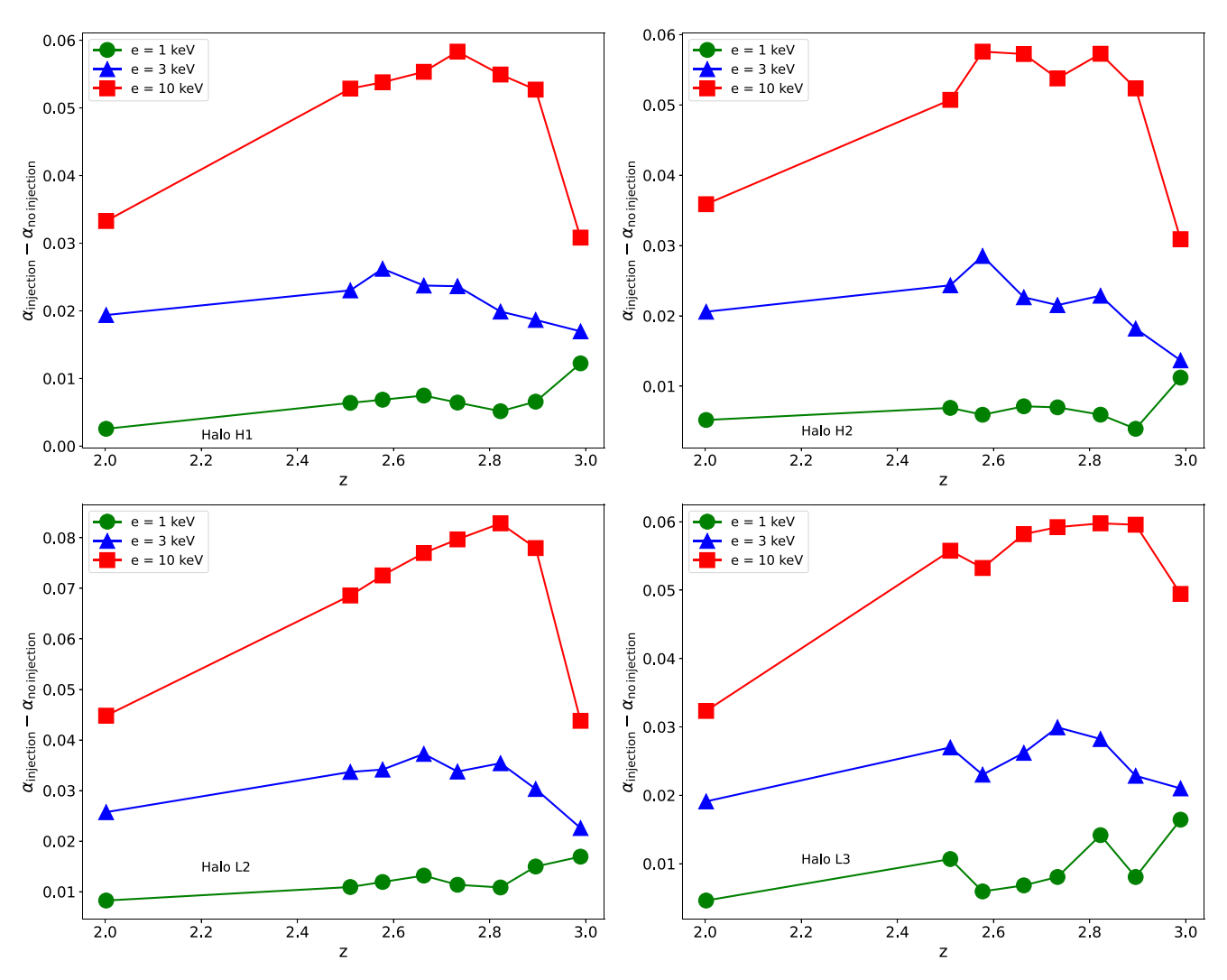


Figure 15. The redshift evolution of the difference in slope between the Ly α transmission—DM density distribution with and without preheating for the protocluster in the remaining halos in the high-resolution simulations with the energy floors. The slopes are measured at the high-density side of the distribution with smoothed DM densities $1 \le \delta_{\rm DM} \le 3$. The panels from left to right and top to bottom show the results of halos H1, H2, L2, and L3, respectively.

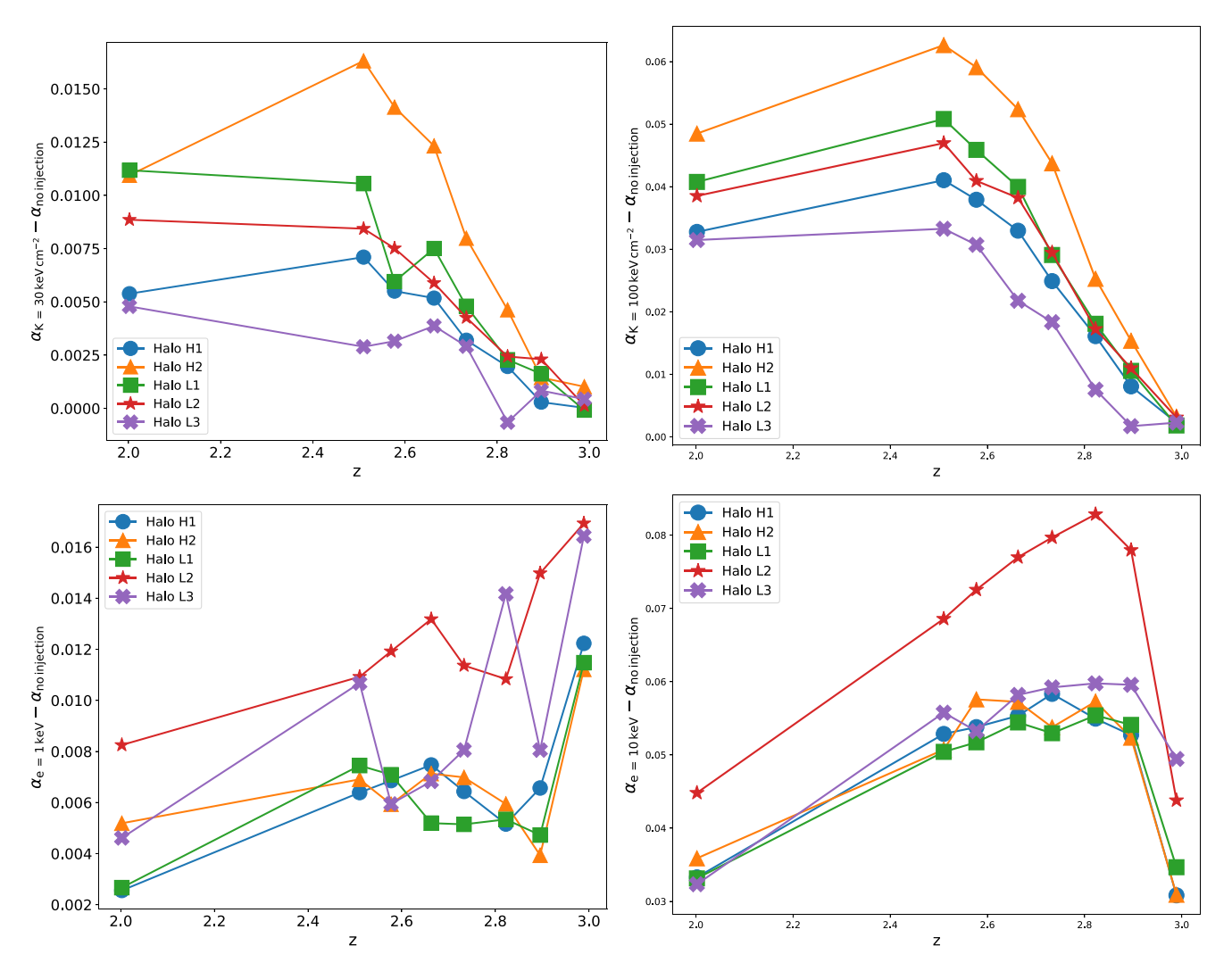


Figure 16. The redshift evolution of the difference in slope between the Ly α transmission—DM density distribution with and without preheating for all of the simulated protoclusters. The slopes are measured at the high-density side of the distribution with smoothed DM densities $1 \le \delta_{\rm DM} \le 3$. The top row shows the results for the low-resolution simulations with the entropy floors of $K_{\rm floor} = 30 \, {\rm keV \, cm^{-2}}$ (left) and $100 \, {\rm keV \, cm^{-2}}$ (right). The bottom row shows results of the high-resolution simulations with the energy floors of $e_{\rm floor} = 3 \, {\rm keV}$ (left) and $10 \, {\rm keV}$ (right).

ORCID iDs

Robin Kooistra https://orcid.org/0000-0002-1008-6675 Shigeki Inoue https://orcid.org/0000-0001-8819-6877 Khee-Gan Lee https://orcid.org/0000-0001-9299-5719 Renyue Cen https://orcid.org/0000-0001-8531-9536 Naoki Yoshida https://orcid.org/0000-0001-7925-238X

References

Arinyo-i-Prats, A., Miralda-Escudé, J., Viel, M., & Cen, R. 2015, JCAP, 2015, 017

Ata, M., Kitaura, F.-S., Lee, K.-G., et al. 2021, MNRAS, 500, 3194

Becker, G. D., Hewett, P. C., Worseck, G., & Prochaska, J. X. 2013, MNRAS, 430, 2067

Bird, S. 2017, FSFE: Fake Spectra Flux Extractor., ascl:1710.012

Borgani, S., Governato, F., Wadsley, J., et al. 2001, ApJL, 559, L71

Borgani, S., & Viel, M. 2009, MNRAS, 392, L26

Bower, R. G., Benson, A. J., Lacey, C. G., et al. 2001, MNRAS, 325, 497

Cai, Z., Fan, X., Peirani, S., et al. 2016, ApJ, 833, 135

Cai, Z., Fan, X., Bian, F., et al. 2017, ApJ, 839, 131

Caucci, S., Colombi, S., Pichon, C., et al. 2008, MNRAS, 386, 211

Cen, R., Miralda-Escudé, J., Ostriker, J. P., & Rauch, M. 1994, ApJL, 437, L9

Chabanier, S., Bournaud, F., Dubois, Y., et al. 2020, MNRAS, 495, 1825

```
Chabanier, S., Palanque-Delabrouille, N., Yèche, C., et al. 2019, JCAP,
   2019, 017
Chaudhuri, A., Majumdar, S., & Nath, B. B. 2013, ApJ, 776, 84
Chaudhuri, A., Nath, B. B., & Majumdar, S. 2012, ApJ, 759, 87
Chiang, Y.-K., Overzier, R. A., Gebhardt, K., & Henriques, B. 2017, ApJL,
   844, L23
Croft, R. A. C., Weinberg, D. H., Katz, N., & Hernquist, L. 1998, ApJ, 495, 44
Cucciati, O., Lemaux, B. C., Zamorani, G., et al. 2018, A&A, 619, A49
de Sainte Agathe, V., Balland, C., du Mas des Bourboux, H., et al. 2019, A&A,
   629, A85
Edge, A. C., & Stewart, G. C. 1991, MNRAS, 252, 414
Evrard, A. E., & Henry, J. P. 1991, ApJ, 383, 95
Hahn, O., & Abel, T. 2011, MNRAS, 415, 2101
Hernquist, L., Katz, N., Weinberg, D. H., & Miralda-Escudé, J. 1996, ApJL,
   457, L51
Iqbal, A., Majumdar, S., Nath, B. B., et al. 2017, MNRAS, 472, 713
Kaiser, N. 1986, MNRAS, 222, 323
Kollmeier, J. A., Miralda-Escudé, J., Cen, R., & Ostriker, J. P. 2006, ApJ,
Kooistra, R., Lee, K.-G., & Horowitz, B. 2022, arXiv:2201.10169
Lee, K.-G., Hennawi, J. F., White, M., Croft, R. A. C., & Ozbek, M. 2014a,
     J. 788, 49
Lee, K.-G., & Spergel, D. N. 2011, ApJ, 734, 21
Lee, K.-G., Hennawi, J. F., Stark, C., et al. 2014b, ApJL, 795, L12
Lee, K.-G., Hennawi, J. F., White, M., et al. 2016, ApJ, 817, 160
Lee, K.-G., Krolewski, A., White, M., et al. 2018, ApJS, 237, 31
```

```
Liang, Y., Kashikawa, N., Cai, Z., et al. 2021, ApJ, 907, 3
Loewenstein, M. 2000, ApJ, 532, 17
Lynds, R. 1971, ApJL, 164, L73
Mandelbaum, R., McDonald, P., Seljak, U., & Cen, R. 2003, MNRAS,
  344, 776
Markevitch, M. 1998, ApJ, 504, 27
McDonald, P., Miralda-Escudé, J., Rauch, M., et al. 2000, ApJ, 543, 1
McDonald, P., Seljak, U., Cen, R., Bode, P., & Ostriker, J. P. 2005, MNRAS,
McQuinn, M. 2016, ARA&A, 54, 313
Meiksin, A. A. 2009, RvMP, 81, 1405
Menci, N., & Cavaliere, A. 2000, MNRAS, 311, 50
Miller, J. S. A., Bolton, J. S., & Hatch, N. A. 2021, MNRAS, 506, 6001
Miralda-Escudé, J., Cen, R., Ostriker, J. P., & Rauch, M. 1996, ApJ, 471, 582
Morganti, R. 2017, FrASS, 4, 42
Nagamine, K., Shimizu, I., Fujita, K., et al. 2021, ApJ, 914, 66
Nanayakkara, T., Glazebrook, K., Kacprzak, G. G., et al. 2016, ApJ, 828, 21
Navarro, J. F., Frenk, C. S., & White, S. D. M. 1995, MNRAS, 275, 720
Nelson, D., Pillepich, A., Genel, S., et al. 2015, A&C, 13, 12
Nelson, D., Springel, V., Pillepich, A., et al. 2019, ComAC, 6, 2
Newman, A. B., Rudie, G. C., Blanc, G. A., et al. 2020, ApJ, 891, 147
Pichon, C., Vergely, J. L., Rollinde, E., Colombi, S., & Petitjean, P. 2001,
   MNRAS, 326, 597
```

```
Pratt, G. W., Arnaud, M., Piffaretti, R., et al. 2010, A&A, 511, A85
Ravoux, C., Armengaud, E., Walther, M., et al. 2020, JCAP, 2020, 010
Rorai, A., Hennawi, J. F., & White, M. 2013, ApJ, 775, 81
Seljak, U., Slosar, A., & McDonald, P. 2006, JCAP, 2006, 014
Shen, L., Lemaux, B. C., Lubin, L. M., et al. 2021, ApJ, 912, 60
Spitler, L. R., Labbé, I., Glazebrook, K., et al. 2012, ApJL, 748, L21
Springel, V. 2010, MNRAS, 401, 791
Stark, C. W., White, M., Lee, K.-G., & Hennawi, J. F. 2015, MNRAS,
  453, 311
Takada, M., Ellis, R. S., Chiba, M., et al. 2014, PASJ, 66, R1
Tonnesen, S., Smith, B. D., Kollmeier, J. A., & Cen, R. 2017, ApJ,
  845, 47
Valageas, P., & Silk, J. 1999, A&A, 350, 725
Viel, M., Schaye, J., & Booth, C. M. 2013, MNRAS, 429, 1734
Vogelsberger, M., Genel, S., Springel, V., et al. 2014a, MNRAS, 444, 1518
Vogelsberger, M., Genel, S., Springel, V., et al. 2014b, Natur, 509, 177
Wang, T., Elbaz, D., Daddi, E., et al. 2016, ApJ, 828, 56
Weinberg, D. H., Davé, R., Katz, N., & Kollmeier, J. A. 2003, in AIP Conf.
  Proc. 666, The Emergence of Cosmic Structure, ed. S. H. Holt &
  C. S. Reynolds (Melville, NY: AIP), 157
Weinberger, R., Springel, V., & Pakmor, R. 2020, ApJS, 248, 32
Wu, K. K. S., Fabian, A. C., & Nulsen, P. E. J. 2000, MNRAS, 318, 889
Zhang, Y., Anninos, P., & Norman, M. L. 1995, ApJL, 453, L57
```